

UniRoute: Unified Routing Mixture-of-Experts for Modality-Adaptive Remote Sensing Change Detection

Qingling Shu^{1*}, Sibao Chen^{1†}, Wei Lu¹, Zhihui You², Chengzhuang Liu¹

¹MOE Key Lab of ICSP, IMIS Lab of Anhui Province, Anhui Provincial Key Lab of Multimodal Cognitive Computation, School of Computer Science and Technology, Anhui University, Hefei, China

²School of Public Safety and Emergency Management, Anhui University of Science and Technology, Hefei, China

Abstract

Current remote sensing change detection (CD) methods mainly rely on specialized models, which limits the scalability toward modality-adaptive Earth observation. For homogeneous CD, precise boundary delineation relies on fine-grained spatial cues and local pixel interactions, whereas heterogeneous CD instead requires broader contextual information to suppress speckle noise and geometric distortions. Moreover, difference operator (e.g. Subtraction) works well for aligned homogeneous images but introduces artifacts in cross-modal or geometrically misaligned scenarios. Across different modality settings, specialized models based on static backbones or fixed difference operations often prove insufficient. To address this challenge, we propose UniRoute, a unified framework for modality-adaptive learning by reformulating feature extraction and fusion as conditional routing problems. We introduce an Adaptive Receptive Field Routing MoE (AR²-MoE) module to disentangle local spatial details from global semantic context, and a Modality-Aware Difference Routing MoE (MDR-MoE) module to adaptively select the most suitable fusion primitive at each pixel. In addition, we propose a Consistency-Aware Self-Distillation (CASD) strategy that stabilizes unified training under data-scarce heterogeneous settings by enforcing multi-level consistency. Extensive experiments on five public datasets demonstrate that UniRoute achieves strong overall performance, with a favorable accuracy–efficiency trade-off under a unified deployment setting.

1 Introduction

Change detection (CD) is a fundamental task in Earth observation [Chang *et al.*, 2021]. With the proliferation of multi-source sensors, real-world applications increasingly demand the processing of diverse data modalities, ranging from homogeneous optical image pairs to heterogeneous combina-

tions like Optical-synthetic aperture radar (SAR) and Optical-Unmanned Aerial Vehicle (UAV). Traditionally, CD models are designed in a specialized manner. For homogeneous CD, siamese architectures with shared encoders and explicit difference operations are commonly adopted to model intensity changes [Fang *et al.*, 2022; Feng *et al.*, 2023; Noman *et al.*, 2024; Li *et al.*, 2025a]. In contrast, heterogeneous CD cannot rely on direct comparison due to pronounced domain gaps. To handle this issue, many approaches use pseudo-siamese fusion networks. These networks learn non-linear semantic mappings or perform style transfer across modalities [Li *et al.*, 2024; Pu *et al.*, 2024; Jing *et al.*, 2025; Wang *et al.*, 2025a]. Although these designs perform well in specific settings (Fig. 1(a)), they typically require separate models for different modality pairs in a unified setting, resulting in increased maintenance and training costs as more modalities are considered.

As shown in Fig. 1(b), unified training exposes challenges that arise in practice. One issue appears during feature extraction and is closely related to receptive field design, which determines the balance between local spatial details and global contextual information. Homogeneous inputs benefit from fine-grained spatial details, which are important for delineating building boundaries. Heterogeneous data present a different situation. For example, Optical–SAR pairs are frequently affected by speckle noise, where broader semantic context becomes more useful than local details. Methods such as A2Net [Li *et al.*, 2023] and PKINet [Cai *et al.*, 2024] combine features produced by convolutional kernels of different sizes. Other architectures, including CDMamba [Zhang *et al.*, 2025] and BSSMamba [Wang *et al.*, 2025b] rely on mechanisms such as modulation or attention to mix local and global information. Although these designs differ in implementation, they all follow a feature integration strategy, which requires the network to accommodate signals with competing characteristics. In SAR data, high-frequency noise captured by local branches can therefore interfere with global semantic representations. Moreover, the behavior of difference operations varies noticeably across modalities. In homogeneous CD, simple pixel-wise interactions often work well, and subtraction can highlight boundary changes. This behavior does not generalize to heterogeneous pairs. For Optical–SAR data, subtraction tends to amplify speckle noise. Geometric misalignment also leads to false responses near object boundaries

*sql@stu.ahu.edu.cn.

†Corresponding author.

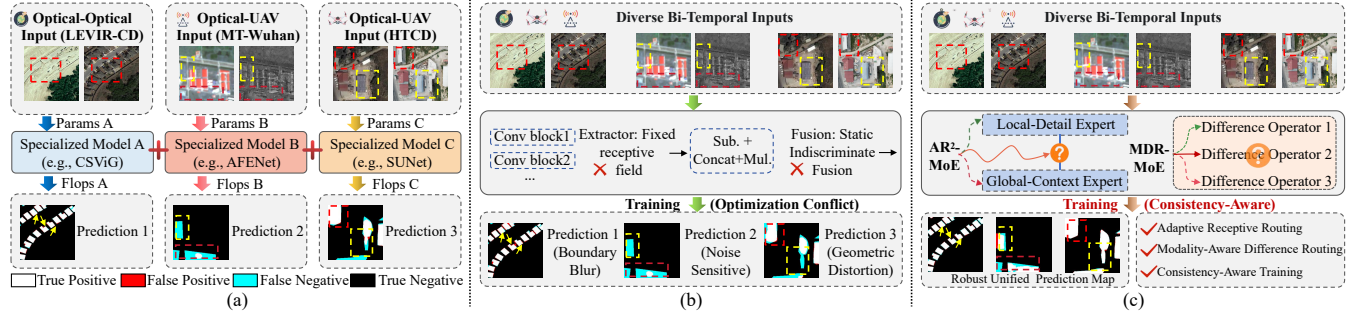


Figure 1: (a) Isolated specialized methods for different modality pairs. (b) Static unified baselines suffering from fixed receptive fields and indiscriminate fusion. (c) Our UniRoute framework with modality-adaptive routing and consistency-aware training.

in Optical-UAV pairs. Some recent methods attempt to reduce this sensitivity by combining multiple operations. Models include CSViG [You *et al.*, 2023] and ChangeCLIP [Dong *et al.*, 2024] aggregate subtraction, concatenation, and related operators within a unified pipeline. This indiscriminate aggregation leads the noisy branches to influence the feature representation when applied in heterogeneous settings.

To address the structural challenges, we argue that a unified model should avoid static compromises. The model should instead act as a dynamic system that can reconfigure itself. Fig. 1(c) illustrates this idea. Inspired by Mixture-of-Experts (MoE) [Shazeer *et al.*, 2017], we propose UniRoute, a modality-adaptive MoE framework built on dynamic routing. We first address the receptive field conflict. We replace standard convolutional blocks with the Adaptive Receptive Field Routing MoE (AR²-MoE). Unlike image-level routing approaches [Chen *et al.*, 2023; Yang *et al.*, 2024], AR²-MoE applies hard routing at the pixel level. This design separates local spatial details, which are critical for boundary detection, from global semantic context, which supports noise suppression. We next consider the operation conflict. We introduce the Modality-Aware Difference Routing MoE (MDR-MoE). MDR-MoE does not combine all fusion primitives by default. Instead, it selects fusion branches based on the input modality. This process removes operations that are likely to introduce noise during feature fusion. Training a unified model across modalities also raises overfitting concerns. This issue is especially severe in data-scarce heterogeneous settings. To mitigate this risk, we propose a Consistency-Aware Self-Distillation (CASD) paradigm. CASD uses self-distillation to enforce geometric invariance. It also introduces decision-level and statistical consistency to stabilize training. Our contributions are summarized as follows:

- We identify the intrinsic conflicts in receptive fields and difference operations for unified CD, and propose UniRoute, a modality-adaptive framework that resolves these conflicts through dynamic expert routing.
- We design AR²-MoE and MDR-MoE, which introduce pixel-wise hard routing to adaptively select optimal spatial contexts and fusion primitives, respectively.
- We propose the CASD training paradigm, which mitigates the small-sample overfitting problem by internalizing multi-level consistency via self-distillation.
- We further demonstrate favorable deployment effi-

ciency: UniRoute supports real-time inference on a single GPU and avoids the system overhead of maintaining or swapping multiple specialized models.

2 Related Work

2.1 Remote Sensing Change Detection

Existing CD methods can be broadly categorized into homogeneous and heterogeneous approaches based on the input modalities. For homogeneous data, siamese networks are the mainstream choice. Methods like TFI-GR [Li *et al.*, 2022], PGPANet [Shu *et al.*, 2024] and DMINet [Feng *et al.*, 2023] employ robust backbone networks to extract features and utilize algebraic subtraction to highlight changes. Recent Transformers [Bandara and Patel, 2022; Chen *et al.*, 2022; Noman *et al.*, 2024] and State Space Models ChangeMamba [Chen *et al.*, 2024] improve long-range context modeling, while SCD-SAM [Mei *et al.*, 2024] utilizes the pre-trained knowledge of the Segment Anything Model for better semantic alignment. Foundation models like Changen2 [Zheng *et al.*, 2025] further leverage large-scale pre-training for universal representations. For heterogeneous data, the domain gap renders simple subtraction ineffective. Methods like SUNet [Shao *et al.*, 2021], ChangeLN [Jing *et al.*, 2024], AFENet [Pu *et al.*, 2024] and HeteCD [Jing *et al.*, 2025] typically rely on style transfer, feature mapping, or metric learning to align multi-modal features. However, these divide-and-conquer methods are unscalable. Homogeneous models fail on SAR data due to noise sensitivity, while heterogeneous models often lack boundary precision on optical imagery. Our UniRoute unifies these scenarios into a single framework, dynamically selecting the optimal difference primitive via the MDR-MoE.

2.2 Mixture-of-Experts in Computer Vision

MoE scales model capacity without increasing inference cost by conditionally activating a subset of experts [Shazeer *et al.*, 2017]. In computer vision, SCNet [Liu *et al.*, 2020] reforms standard convolutions via a self-calibration operation that expands the field-of-view. Recent vision MoEs (e.g., AdaMViMoE [Chen *et al.*, 2023], MLoRE [Yang *et al.*, 2024]) have explored image-level or patch-level routing. DAMEX [Jain *et al.*, 2024] introduces dataset-aware routing for universal object detection. However, most approaches employ soft gating or shared expert architectures (e.g., identical convolution

blocks), which leads to feature blurring and insufficient specialization. This is critical for dense prediction tasks like CD, where precise boundary delineation is paramount. In contrast, our AR²-MoE introduces a pixel-wise hard routing mechanism via the Straight-Through Estimator (STE) [Jang *et al.*, 2017]. Unlike coarse-grained routing that may introduce block artifacts, our method achieves fine-grained adaptation by explicitly disentangling high-frequency local details from global context at every spatial location, resolving the receptive field conflict inherent in multi-modal data.

2.3 Unified Modeling & Training Strategies

Developing a unified model for diverse tasks is a long-standing goal. Pioneering work like Perceiver IO [Jaegle *et al.*, 2022] utilizes a shared Transformer backbone to handle multi-modal inputs via tokenization. In remote sensing, SM3Det [Li *et al.*, 2025b] explores unified object detection across optical and SAR domains. A key challenge in unified training is the optimization conflict arising from task heterogeneity. While multi-task learning methods address this by balancing gradients [Chen *et al.*, 2018], and Test-Time Adaptation (TTA) [Wang *et al.*, 2021] improves robustness during inference, these approaches often require complex optimization or online updates. Alternatively, we propose a CASD paradigm. Instead of heavy optimization tricks, we leverage self-supervised geometric consistency to regularize training.

3 Methodology

3.1 Overview

Given a collection of remote sensing CD datasets $\mathcal{D} = \{D_1, \dots, D_N\}$, where each sample consists of a bi-temporal image pair $(\mathbf{T}_1, \mathbf{T}_2)$ and a change map \mathbf{GT} . The modalities of \mathbf{T}_1 and \mathbf{T}_2 can be either homogeneous (e.g., Optical-Optical) or heterogeneous (e.g., Optical-UAV, Optical-SAR). We propose UniRoute, a unified modality-adaptive framework shown in Fig. 2. It introduces the AR²-MoE to disentangle receptive field requirements and the MDR-MoE to dynamically select optimal fusion primitives. Furthermore, to mitigate overfitting on small-sample heterogeneous datasets, we introduce a CASD training paradigm, which internalizes geometric invariance and aligns cross-modal semantics.

3.2 Adaptive Receptive Field Routing MoE

To address modality-dependent receptive field conflicts, we introduce AR²-MoE, which treats receptive field selection as an input-conditioned routing problem. Rather than statically aggregating multi-scale features, AR²-MoE performs pixel-wise hard routing between two experts with complementary receptive field properties, allowing each spatial location to adaptively select an appropriate context.

Decoupled Receptive-Field Experts. Given the intermediate feature map $\mathbf{F}_s^1, \mathbf{F}_s^2 \in \mathbb{R}^{B \times C_s \times H_s \times W_s}$ form the temporal branch $s \in \{1, 2, 3, 4\}$, we omit batch and stage indices for brevity and denote the input as \mathbf{X} . The AR²-MoE aims to learn a dynamic mapping by selectively activating experts from a decomposed functional space. We construct two experts with complementary receptive field behaviors. The

Local-Detail Expert focuses on preserving fine-grained spatial structures using a compact convolutional operator, which is effective for boundary-sensitive optical imagery.

$$E_{lde}(\mathbf{X}) = \Phi_{local}(\mathbf{X}; \mathbf{W}_{3 \times 3}), \quad (1)$$

where Φ_{local} denotes a depth-wise separable convolution block with a small kernel size. The *Global-Context Expert* uses a dilated, decomposed convolution sequence to emphasize broader contextual information, helping reduce modality-specific noise such as SAR speckle. Instead of computationally prohibitive self-attention, we approximate global dependencies via a decomposed convolution sequence:

$$E_{gce}(\mathbf{X}) = \mathcal{F}_{pw}(\mathcal{F}_{dilated}(\mathcal{F}_{dw}(\mathbf{X}))) \odot \mathbf{X}, \quad (2)$$

where \mathcal{F}_{dw} denotes a depth-wise convolution, $\mathcal{F}_{dilated}$ is a depth-wise dilated convolution with dilation rate $d = 3$ and \mathcal{F}_{pw} represents a point-wise convolution for channel mixing. The operator \odot represents element-wise modulation. With this decomposition, the expert primarily attends to features from a large receptive field. This reduces the influence of local noise and preserves the global semantic information.

Entropy-Constrained Hard Routing. To dynamically assign these experts, we employ a grid-level gating network G conditioned on local visual features \mathbf{X} :

$$\mathbf{g} = \sigma(\mathcal{W}_g(\gamma(\mathbf{z}) \odot \phi(\mathbf{X}) + \beta(\mathbf{z}))). \quad (3)$$

Here, $\phi(\cdot)$ denotes a lightweight feature projection implemented as a 1×1 convolution, and $\gamma(\mathbf{z})$ and $\beta(\mathbf{z})$ perform channel-wise modulation on the projected features, while the gating weights \mathcal{W}_g map the modulated features to expert selection logits. σ is the Sigmoid function and \mathbf{z} is a domain code representing the source domain, which is available as domain metadata and used as a conditioning prior. We find that soft gating can mix the responses of different experts, making their roles less distinct. To preserve expert specialization, we use discrete hard routing based on the Straight-Through Estimator (STE). The binary routing mask \mathbf{M} is computed as:

$$\mathbf{M} = \mathbb{I}(\mathbf{g} > 0.5) - \text{detach}(\mathbf{g}) + \mathbf{g}, \quad (4)$$

where $\mathbb{I}(\cdot)$ is the indicator function. The term $\text{detach}(\mathbf{g})$ stops the gradient flow, allowing \mathbf{M} to behave as a binary mask during the forward pass while enabling gradients to flow through the continuous probability \mathbf{g} during backward propagation. We adopt STE-based hard routing to enable discrete expert selection while maintaining end-to-end differentiability. During training, routing decisions are binary in the forward pass, while gradients are propagated through the continuous gating probabilities. The final output is dynamically assembled:

$$\mathbf{y} = (1 - \mathbf{M}) \odot E_{lde}(\mathbf{X}) + \mathbf{M} \odot E_{gce}(\mathbf{X}) + \mathbf{X}. \quad (5)$$

This design ensures that in ambiguous regions where experts might provide conflicting signals, the network preserves the original feature identity \mathbf{X} , stabilizing the gradient flow.

3.3 Modality-Aware Difference Routing MoE

Difference modeling in unified CD is highly modality-dependent. Static fusion of multiple operators often leads to

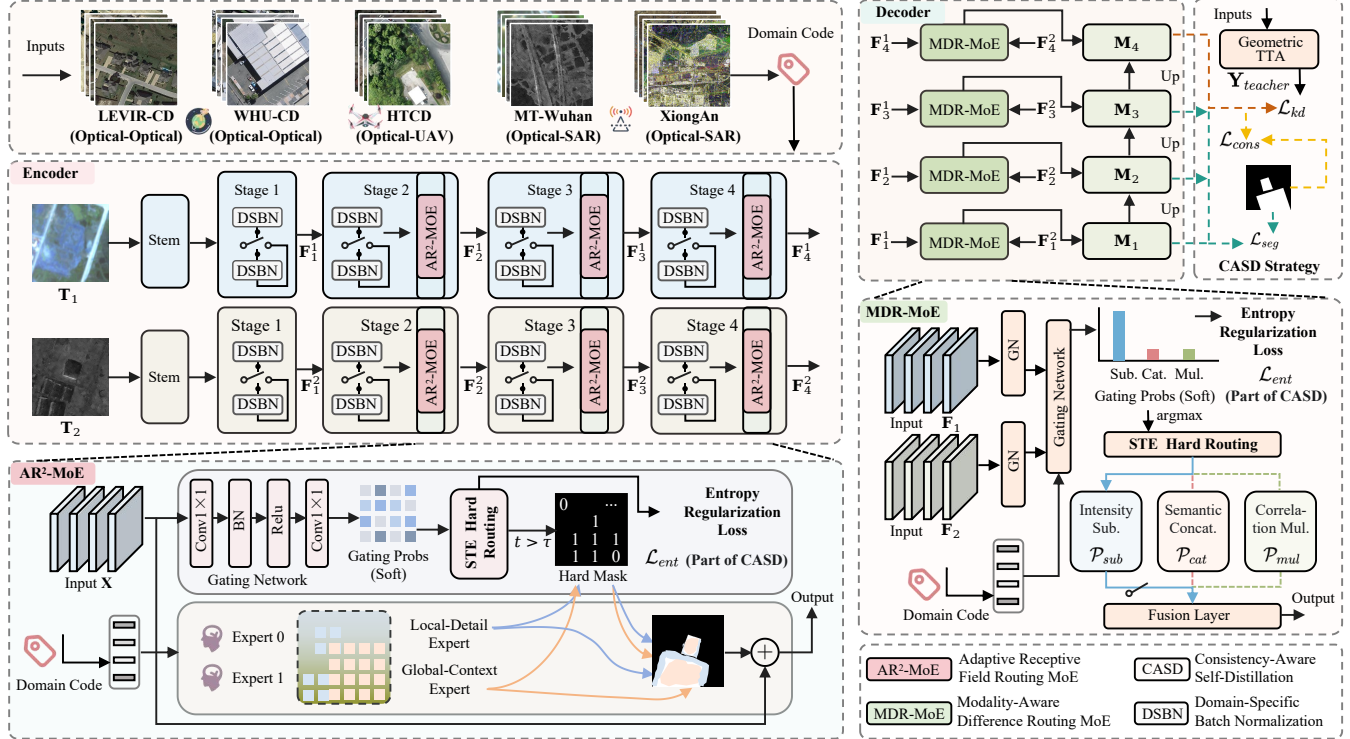


Figure 2: Overview of UniRoute. It features an AR²-MoE for adaptive receptive field selection in the encoder and an MDR-MoE for optimal fusion primitive routing in the decoder, optimized via the CASD strategy.

incompatible responses across heterogeneous inputs. To address this issue, we propose MDR-MoE, which formulates difference modeling as a conditional routing problem.

Library of Differentiable Primitives. Given bi-temporal features $\mathbf{F}_s^1, \mathbf{F}_s^2$ at stage s , we simplify the notation to $\mathbf{F}_1, \mathbf{F}_2$. To enable modality-dependent selection rather than indiscriminate fusion, we construct a compact library of differentiable primitives, each encoding a distinct inductive bias for change modeling. Formally, we denote the primitive set as $\mathcal{P} = \{\mathcal{P}_k\}_{k=1}^K$, including subtraction, concatenation, and multiplicative interaction. Each primitive captures a distinct inductive bias for change modeling, and a lightweight projection layer is applied for feature alignment.

Modality-Aware Hard Routing. Instead of indiscriminate fusion, which cannot resolve operation conflicts across modalities, MDR-MoE employs a discrete routing mechanism. We utilize a gating network G to predict the selection probability $\Pi \in \mathbb{R}^{B \times K \times H \times W}$ based on the input features and a domain code.

$$\Pi = \sigma\left(\mathcal{W}_g\left(\gamma(\mathbf{z}) \odot \phi([\mathbf{F}_1, \mathbf{F}_2]) + \beta(\mathbf{z})\right)\right), \quad (6)$$

Here, \mathbf{z} is shared with AR²-MoE as a domain conditioning code to ensure consistent operator selection. To ensure strict operation decoupling (i.e., actively pruning noisy branches), we apply Top-1 Hard Routing via the STE. The binary selection mask $\mathbf{Z} \in \{0, 1\}^{B \times K \times H \times W}$ is:

$$\mathbf{Z} = \text{OneHot}(\arg \max_k(\Pi)) - \text{detach}(\Pi) + \Pi. \quad (7)$$

The final difference feature \mathbf{M}_{diff} is dynamically assembled

by selecting the optimal primitive for each spatial location:

$$\mathbf{M}_{diff} = \sum_{k=1}^K \mathbf{Z}_k \odot \mathcal{P}_k(\mathbf{F}_1, \mathbf{F}_2), \quad (8)$$

where \mathbf{Z}_k is the one-hot hard mask for the k -th primitive (corresponding to $\mathcal{P}_{sub}, \mathcal{P}_{cat}, \mathcal{P}_{mul}$, respectively). With the proposed routing, subtraction is used for aligned homogeneous inputs, while fusion-based primitives are applied to heterogeneous or geometrically misaligned data in the same model.

3.4 Consistency-Aware Self-Distillation (CASD)

Training a unified model on heterogeneous datasets is challenging due to inconsistent supervision across modalities under limited data, which leads to unstable optimization and unreliable expert routing. We introduce CASD as a training regularization strategy to stabilize optimization by enforcing multi-level consistency.

Geometric Consistency via Self-Distillation. Standard supervision is sensitive to geometric variations and easily overfits in data-scarce settings. We therefore enforce prediction consistency under spatial transformations through self-distillation with Test-Time Augmentation (TTA). Specifically, given a transformation \mathcal{T} (e.g., horizontal flip), the model aggregates predictions from the original and transformed views to construct a robust soft target:

$$\mathbf{Y}_{teacher} = \frac{1}{2}(\sigma(\mathcal{M}(\mathbf{T}_1, \mathbf{T}_2)) + \mathcal{T}^{-1}(\sigma(\mathcal{M}(\mathcal{T}(\mathbf{T}_1, \mathbf{T}_2))))). \quad (9)$$

Here, \mathcal{M} denotes the model and \mathcal{T}^{-1} represents the inverse spatial transformation to align the predictions. The student model (standard forward pass) is then optimized via MSE loss to match this soft target:

$$\mathcal{L}_{kd} = \|\sigma(\mathcal{M}(\mathbf{X})) - \mathbf{Y}_{teacher}\|^2, \quad (10)$$

which internalizes geometric invariance into the model weights and mitigates overfitting on small-sample datasets.

Decision Consistency for Confident Supervision. Effective distillation relies on the teacher providing sharp, unambiguous guidance. However, data scarcity often leads to routing ambiguity, where the teacher hesitates between experts. To ensure the teacher generates decisive guidance, we introduce an entropy regularization term on the gating distribution:

$$\mathcal{L}_{ent} = -\frac{1}{|\Omega|} \sum_{u \in \Omega} \sum_{k=1}^K p_{u,k} \log(p_{u,k} + \epsilon), \quad (11)$$

where Ω denotes the spatial domain and K is the number of experts. Minimizing this entropy term encourages low-entropy, confident routing decisions, thereby promoting sparse, near-binary expert selection and structurally distinct distilled knowledge.

Representation & Statistical Consistency. Reliable knowledge transfer further requires stable feature representations. We apply a feature-level consistency loss that minimizes the cosine distance of deep features in unchanged areas Ω_0 :

$$\mathcal{L}_{cons} = \frac{1}{|\Omega_0|} \sum_{u \in \Omega_0} \left(1 - \frac{\mathbf{F}_1(u) \cdot \mathbf{F}_2(u)}{\|\mathbf{F}_1(u)\|_2 \|\mathbf{F}_2(u)\|_2} \right), \quad (12)$$

where $\mathbf{F}_1(u)$ and $\mathbf{F}_2(u)$ denote the feature vectors at spatial location u from the two input images. To prevent domain shifts from disrupting this representation alignment, we adopt Domain-Specific Batch Normalization (DSBN), which follows standard hard domain routing during training, while enabling adaptive normalization selection at inference. For each modality d , DSBN maintains independent affine parameters $\{\gamma^{(d)}, \beta^{(d)}\}$ and running statistics $\{\mu^{(d)}, \sigma^{(d)}\}$.

$$DSBN(x^{(d)}) = \gamma^{(d)} \frac{x^{(d)} - \mu^{(d)}}{\sqrt{(\sigma^{(d)})^2 + \epsilon}} + \beta^{(d)}. \quad (13)$$

This isolation prevents the statistical distribution of one modality (e.g., speckle noise in SAR) from contaminating others, creating a stable environment for unified optimization. The final training objective aggregates these multi-level consistency constraints:

$$\mathcal{L}_{total} = \mathcal{L}_{seg} + \lambda_{cons} \mathcal{L}_{cons} + \lambda_{kd} \mathcal{L}_{kd} + \lambda_{ent} \mathcal{L}_{ent}, \quad (14)$$

where \mathcal{L}_{seg} is the segmentation loss and λ terms balance the auxiliary objectives. In practice, the auxiliary losses are activated in a stage-wise manner. During unified pre-training, we optimize \mathcal{L}_{seg} together with \mathcal{L}_{cons} and \mathcal{L}_{ent} to stabilize expert routing. During the CASD fine-tuning stage, \mathcal{L}_{ent} is removed and \mathcal{L}_{kd} is introduced to perform self-distillation under geometric transformations.

4 Experiments and Analysis

4.1 Datasets and Implementation Details

We evaluate our UniRoute on five public datasets: LEVIR-CD [Chen and Shi, 2020] and WHU-CD [Ji *et al.*, 2018] (Optical-Optical); HTCD [Shao *et al.*, 2021] (Optical-UAV); and MT-Wuhan [Zhang *et al.*, 2022] and XiongAn [Jing *et al.*, 2025] (heterogeneous Optical-SAR). We use a ResNet50 [He *et al.*, 2016] backbone pretrained on ImageNet. Training follows a two-stage paradigm: (1) *Unified Pre-training* for 200 epochs on combined datasets using AdamW (learning rate = 3×10^{-4}); (2) *CASD Fine-tuning* for 15 epochs with reduced lr (1×10^{-5}) and re-balanced sampling for small-sample datasets. We report F1-score and IoU on the test sets using the best validation checkpoint. For fair comparison, all baseline methods are re-implemented using their official codebases and standard protocols. Note that we do not apply CASD to baselines. This is because CASD is tailored to regularize dynamic routing instability; applying strict geometric consistency to static backbones often leads to optimization conflicts or marginal gains in our preliminary tests. More details are in the Supplementary Material.

4.2 Comparison with State-of-the-Art Methods

We compare UniRoute with recent SOTA methods, including CSViG [You *et al.*, 2023], ChangeMamba [Chen *et al.*, 2024], LGCANet [Jiang and Wu, 2025], LWGANet [Lu *et al.*, 2025], AFENet [Pu *et al.*, 2024], Bi-DiffCD [Zhao *et al.*, 2025], HRSICD [Wang *et al.*, 2025a] and HeteCD [Jing *et al.*, 2025]. Tab. 1 shows the quantitative results. More details are in the Supplementary Material.

Comparison with Specialized Models. Specialized models perform well in narrow domains, but they lack versatility. For example, LWGANet achieves a high F1 score of 92.42% on LEVIR-CD. However, the same model drops sharply to 55.78% on MT-Wuhan. To reach the coverage of UniRoute, one would need an ensemble of best specialists. This ensemble requires 132.1M parameters and 332.7G FLOPs while our UniRoute breaks this trade-off. With only 52.9M parameters, UniRoute matches the ensemble in average performance. It achieves an Avg F1 of 85.10%, compared to 84.76% for the ensemble. As a result, our model achieves SOTA accuracy with only 40% of the parameters and 10% of the FLOPs of the ensemble.

Comparison with Unified Baselines. We observe that re-training SOTA models on mixed datasets frequently leads to performance degradation due to negative transfer. ChangeMamba drops from 91.18% to 89.35% on LEVIR-CD and from 56.44% to 53.88% on MT-Wuhan in the unified setting. In contrast, UniRoute remains robust, which outperforms the best unified baseline (AFENet) by 4.64% on average. The gains on MT-Wuhan (+4.32%) and HTCD (+7.82%) highlight the efficacy of dynamic routing in resolving conflicts.

Qualitative Analysis. As shown in Fig. 3, On homogeneous LEVIR-CD and WHU-CD datasets, ChangeMamba and CSViG often exhibit blurred boundaries and noticeable prediction errors. For heterogeneous scenarios (e.g. MT-Wuhan), AFENet misclassifies speckle noise as changes. In contrast, UniRoute delivers clean shapes and preserves fine-

| Model | Setting | Params | FLOPs | LEVIR-CD | | WHU-CD | | HTCD | | MT-Wuhan | | XiongAn | | Avg F1 \uparrow |
|--|---------|------------------|------------------|---------------|----------------|---------------|----------------|---------------|----------------|---------------|----------------|---------------|----------------|-------------------|
| | | (M) \downarrow | (G) \downarrow | F1 \uparrow | IoU \uparrow | |
| <i>Single-Modal Specialists (Trained Individually)</i> | | | | | | | | | | | | | | |
| BCD | | | | | | | | | | | | | | |
| CSViG (TGRS 23) | Indiv. | 38.0 | 203.0 | 91.52 | 84.37 | 90.57 | 82.76 | 91.16 | 83.76 | 54.80 | 37.74 | 75.17 | 60.22 | 80.64 |
| ChangeMamba (TGRS 24) | Indiv. | 84.7 | 179.3 | 91.18 | 83.80 | 94.19 | 89.02 | 92.54 | 86.12 | 56.44 | 39.31 | 78.63 | 64.78 | 82.60 |
| LGCANet (TGRS 25) | Indiv. | 31.0 | 56.6 | 89.96 | 81.75 | 94.23 | 89.09 | 90.90 | 83.52 | 52.21 | 35.33 | 78.95 | 65.22 | 81.25 |
| LWGANet (AAAI 26) | Indiv. | 16.1 | 22.1 | 92.42 | 85.90 | 95.24 | 90.92 | 92.21 | 85.55 | 55.78 | 38.68 | 79.48 | 65.94 | 83.03 |
| <i>MCD</i> | | | | | | | | | | | | | | |
| AFENet (TGRS 24) | Indiv. | 39.7 | 99.6 | 89.61 | 81.18 | 92.39 | 85.86 | <u>95.73</u> | <u>91.82</u> | <u>59.82</u> | <u>42.67</u> | 80.20 | 66.95 | <u>83.55</u> |
| Bi-DiffCD (IJCAI 25) | Indiv. | 68.3 | 76.5 | 89.86 | 81.58 | 93.49 | 87.78 | 92.54 | 86.12 | 52.60 | 35.69 | 79.13 | 65.47 | 81.52 |
| HRSICD (ISPRS 25) | Indiv. | 20.5 | 89.3 | 89.42 | 80.87 | 92.86 | 86.67 | 93.11 | 87.10 | 54.82 | 37.76 | 80.60 | <u>67.50</u> | 82.16 |
| HeteCD (ISPRS 25) | Indiv. | 50.2 | 58.2 | 90.20 | 82.19 | 93.36 | 87.55 | 94.34 | 89.30 | 56.38 | 39.25 | 80.34 | 67.14 | 82.92 |
| Ensemble of Best Specialists | Indiv. | 132.1 | 332.7 | 92.42 | 85.90 | 95.24 | 90.92 | 95.73 | 91.82 | 59.82 | 42.67 | 80.60 | 67.50 | 84.76 |
| <i>Unified Baselines (Re-implemented)</i> | | | | | | | | | | | | | | |
| BCD | | | | | | | | | | | | | | |
| CSViG (TGRS 23) \dagger | Unified | 31.0 | 203.0 | 89.84 | 81.56 | 88.47 | 79.33 | 85.01 | 73.93 | 51.54 | 34.71 | 78.18 | 64.17 | 78.61 |
| ChangeMamba (TGRS 24) \dagger | Unified | 84.7 | 179.3 | 89.35 | 80.75 | 92.88 | 86.70 | 87.43 | 77.66 | 53.88 | 36.87 | 76.43 | 61.85 | 79.99 |
| LGCANet (TGRS 25) \dagger | Unified | 31.0 | 56.6 | 88.42 | 79.25 | 91.00 | 83.48 | 84.75 | 73.53 | 49.68 | 33.05 | 75.49 | 60.63 | 77.87 |
| LWGANet (AAAI 26) \dagger | Unified | 16.1 | 22.1 | 90.32 | 82.35 | 93.48 | 87.70 | 86.84 | 76.75 | 52.38 | 35.48 | 76.77 | 62.29 | 79.96 |
| <i>MCD</i> | | | | | | | | | | | | | | |
| AFENet (TGRS 24) \dagger | Unified | 39.7 | 99.6 | 88.49 | 79.36 | 90.36 | 82.42 | 88.62 | 79.56 | 56.11 | 39.19 | 78.71 | 64.89 | 80.46 |
| Bi-DiffCD (IJCAI 25) \dagger | Unified | 68.3 | 76.5 | 88.30 | 79.05 | 91.64 | 84.57 | 84.68 | 73.42 | 50.42 | 33.72 | 77.68 | 63.50 | 78.54 |
| HRSICD (ISPRS 25) \dagger | Unified | 20.5 | 89.3 | 88.05 | 78.66 | 91.29 | 83.98 | 85.23 | 74.26 | 53.58 | 36.60 | 79.51 | 65.99 | 79.53 |
| HeteCD (ISPRS 25) \dagger | Unified | 50.2 | 58.2 | 89.14 | 80.40 | 91.41 | 84.18 | 86.62 | 76.40 | 53.56 | 36.57 | 78.84 | 65.07 | 79.91 |
| Ours \dagger | Unified | 52.9 | 35.5 | <u>91.93</u> | <u>85.06</u> | 95.26 | 90.94 | 96.44 | 93.13 | 60.43 | 43.29 | 81.46 | 68.71 | 85.10 |

Table 1: Comparison with state-of-the-art methods. We compare our unified UniRoute against both specialized models (trained individually) and unified baselines (re-implemented under our unified protocol). \dagger denotes unified training setting. The best and second-best results are highlighted in **bold** and underlined. All metrics are expressed as percentages (%).

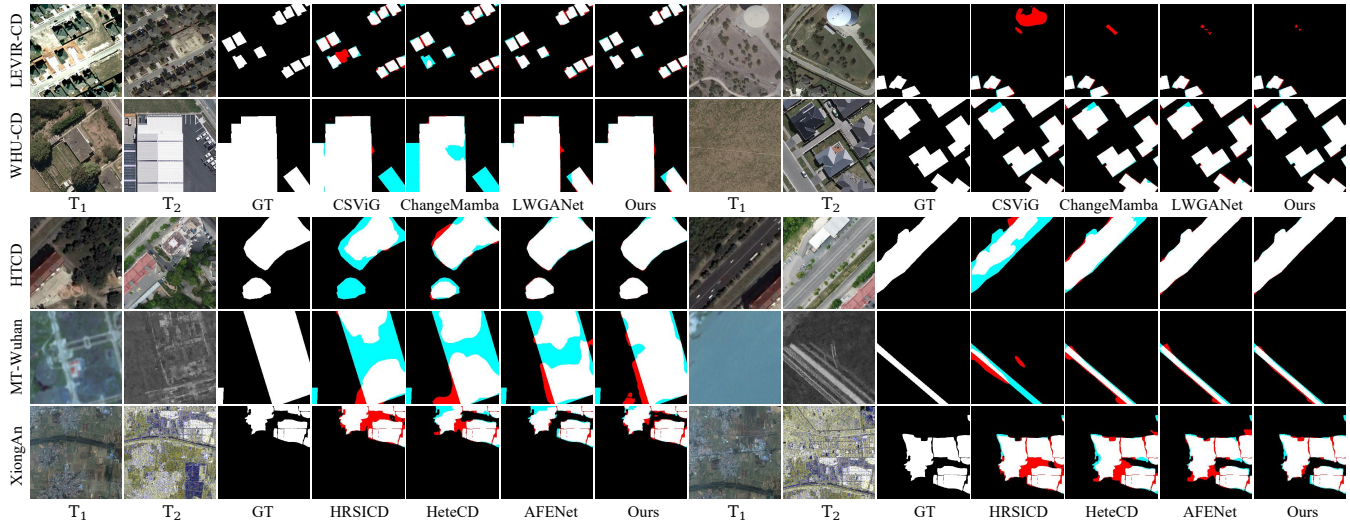


Figure 3: Qualitative comparisons on five datasets. We show predicted change maps of representative methods and our UniRoute on both homogeneous and heterogeneous settings.

grained edges. Notably, in HTCD, our model maintains robust alignment despite viewpoint distortions, avoiding false alarms common in subtraction-based approaches.

4.3 Ablation Study

As shown in Tab. 2, we conduct ablation studies on the representative datasets LEVIR-CD, HTCD, and MT-Wuhan to analyze model behavior under different settings. More details are in the Supplementary Material.

Effectiveness of AR²-MoE. To demonstrate the effectiveness of AR²-MoE, we first remove AR²-MoE from the network. Tab. 2 reports the corresponding results. This design causes

a slight performance drop on LEVIR-CD and WHU-CD, but leads to a degradation on MT-Wuhan, where the F1 decreases to 55.8%. As shown in Row #2-#4, introducing AR²-MoE leads to consistent performance gains. We tend to insert AR-MoE at different stages of the network. The experiments show that the accuracy consistently improves as AR-MoE is introduced. Considering the trade-off between computational cost and accuracy, we place AR-MoE only at the deeper Stages 2-4. Rows #05 and #06 further show that relying on a single expert alone, either local-detail or global-context, is insufficient to handle heterogeneous scenes, highlighting the necessity of dynamic expert selection. Multi-kernel fusion

| NO. | Variants | LEVIR-CD | HTCD | MT-Wuhan |
|--------------------------------|--|--------------|--------------|--------------|
| #00 | UniRoute (Ours) | 91.93 | 96.44 | 60.43 |
| <i>(a) AR²-MoE</i> | | | | |
| #01 | w/o AR ² -MoE (Vanilla ResNet) | 90.34 | 95.30 | 55.80 |
| #02 | w/ AR ² -MoE (Stage 4 only) | 91.45 | 95.65 | 57.20 |
| #03 | w/ AR ² -MoE (Stage 3, 4) | 91.68 | 96.10 | 58.90 |
| #04 | w/ AR ² -MoE (Stage 1, 2, 3, 4) | 91.86 | 96.40 | 59.79 |
| #05 | w/ Only <i>Local-Detail Expert</i> | 91.45 | 95.80 | 56.20 |
| #06 | w/ Only <i>Global-Context Expert</i> | 90.22 | 95.10 | 59.80 |
| #07 | w/ Multi-Kernel (3x3 + 5x5 + 7x7) | 90.70 | 95.60 | 58.45 |
| <i>(c) MDR-MoE</i> | | | | |
| #08 | w/o MDR-MoE (Naive Concat) | 90.50 | 95.80 | 56.50 |
| #09 | w/ Sub. Only (Static) | 91.55 | 90.50 | 42.10 |
| #10 | w/ Cat. Only (Static) | 90.40 | 95.63 | 58.50 |
| #11 | w/ Mul. Only (Static) | 89.20 | 91.23 | 54.00 |
| #12 | w/ DFC (Sub+Cat+Mul) | 91.60 | 94.87 | 57.80 |
| <i>(d) CASD</i> | | | | |
| #13 | w/o CASD (Standard Training) | 91.80 | 96.20 | 57.78 |
| <i>(e) Different Backbones</i> | | | | |
| #14 | ResNet18 | 90.10 | 94.50 | 54.20 |
| #15 | ResNet34 | 91.20 | 95.80 | 58.10 |
| #16 | ResNet50 (Ours) | 91.93 | 96.44 | 60.43 |
| #17 | Swin-T | 91.60 | 96.00 | 57.50 |

Table 2: Ablation study on key components and architectures.

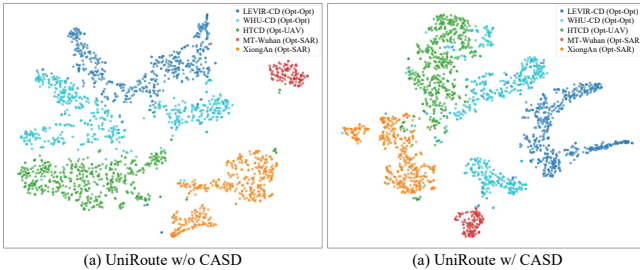


Figure 4: t-SNE visualization of feature distributions.

(Row #07) improve capacity by combining multiple receptive fields, but they indiscriminately apply the same fusion. By contrast, AR²-MoE uses conditional routing to adapt the receptive field on a per-pixel basis, allowing different regions to rely on receptive fields of appropriate scales.

Effectiveness of MDR-MoE. To demonstrate the effectiveness of MDR-MoE, we first remove MDR-MoE from the network. The performance drops on all three datasets. As shown in Row #9–#11, different modalities favor different difference operators. The subtraction operator performs well on the homogeneous LEVIR-CD dataset. However, its performance on MT-Wuhan drops sharply to 42.1%. This result indicates that SAR features introduce strong noise during differencing. To compare MDR-MoE with existing difference operators, we replace our design with the DFC module from ChangeCLIP. DFC integrates multiple operators into a unified difference module. Row #12 shows that DFC achieves competitive performance. However, our method still outperforms DFC by 1.57% on HTCD and 2.63% on MT-Wuhan. This shows that the limitation lies not in the primitives themselves but in the fusion strategy: statically including noisy branches contaminates features, whereas MDR-MoE effectively prunes them.

Effectiveness of CASD. As shown in Row #13, we first remove the CASD training strategy. Tab. 2 shows that the performance on LEVIR-CD and HT-CD drops only slightly. However, the performance on MT-Wuhan decreases to 57.78%. This result further confirms that CASD prevents overfitting on small-scale heterogeneous datasets while pro-

| Routing Mechanism | Differentiable | LEVIR-CD | HTCD | MT-Wuhan |
|--------------------------------|----------------|--------------|--------------|--------------|
| Soft Gating (Weighted Sum) | ✓ | 91.50 | 96.15 | 58.50 |
| Top-1 Hard (No STE) | ✗ | 88.40 | 92.10 | 52.10 |
| Gumbel-Softmax | ✓ | 91.65 | 96.22 | 59.20 |
| STE Hard Routing (Ours) | ✓ | 91.93 | 96.44 | 60.43 |

Table 3: Analysis of routing strategies.

| Initialization | Data Fraction | Epochs | F1 | Δ |
|------------------------------|-------------------|-----------|--------------|--------------|
| ImageNet Init. | 5% (~800 pairs) | 50 | 69.25 | - |
| UniRoute Init. (Ours) | 5% | 20 | 74.88 | +5.63 |
| ImageNet Init. | 10% (~1600 pairs) | 50 | 74.97 | - |
| UniRoute Init. (Ours) | 10% | 20 | 77.48 | +3.16 |

Table 4: Few-Shot transfer learning on unseen SYSU-CD dataset.

vides positive gains on other datasets. It is noted UniRoute *without* CASD still outperforms the strongest unified baseline (AFENet) on challenging heterogeneous datasets (e.g., 57.78% vs. 56.11% on MT-Wuhan), confirming that our architectural advantage is intrinsic. The t-SNE visualization in Fig. 4 supports this conclusion. CASD training strategy effectively reduces modality discrepancies. The embeddings of homogeneous and heterogeneous datasets become closer in the feature space.

Backbone Scalability. We replace the backbone of UniRoute with different architectures, including ResNet variants and transformer. Rows #14–#17 in the table report the corresponding results. ResNet-50 and Swin-T achieve the best overall performance. Considering the trade-off between accuracy, parameter count, and computational cost, we adopt ResNet-50 as the backbone in this work.

Routing Strategies Analysis. To evaluate the impact of different gating strategies, we replace STE with alternative designs. The results in Tab. 3 show that standard soft gating achieves reasonable performance. However, this strategy performs poorly on heterogeneous data such as Optical-SAR. Top-1 selection without STE fails to converge due to gradient blocking and yields low accuracy. By introducing STE, our method enables end-to-end training with discrete selection. This design balances sparsity and differentiability, which achieves the best performance.

4.4 Generalization and Data Efficiency

Due to severe domain shift and modality-specific noise, fully zero-shot CD across modalities is highly challenging. Therefore, we conduct few-shot transfer experiments in this work. We fine-tune the model on the previously unseen SYSU dataset using limited training data. The experimental results in Tab. 4 show that our method achieves a 5.63% improvement over ImageNet initialization when using only 5% of the data. These results indicate that our model learns change representations with strong cross-dataset transferability.

5 Conclusion

In this paper, we identify the intrinsic conflicts in receptive fields and fusion operations that hinder unified CD. To resolve them, we propose UniRoute, a modality-adaptive framework that formulates feature extraction and fusion as a conditional routing problem. Through AR²-MoE and MDR-MoE, our

model adaptively selects receptive fields and optimal fusion primitives to accommodate heterogeneous characteristics at the pixel level. Furthermore, we introduce a CASD strategy to regularize training under data-scarce and heterogeneous settings by enforcing multi-level consistency. Extensive experiments show that UniRoute consistently outperforms unified baselines and remains competitive with strong specialists, while keeping a single unified model that is efficient in both parameters and computation.

References

[Bandara and Patel, 2022] Wele Gedara Chaminda Bandara and Vishal M. Patel. A transformer-based siamese network for change detection. In *IGARSS 2022 - 2022 IEEE International Geoscience and Remote Sensing Symposium*, pages 207–210, 2022.

[Cai *et al.*, 2024] Xinhao Cai, Qiuxia Lai, Yuwei Wang, Wenguan Wang, Zeren Sun, and Yazhou Yao. Poly kernel inception network for remote sensing detection. In *2024 IEEE/CVF Conference on Computer Vision and Pattern Recognition (CVPR)*, pages 27706–27716, 2024.

[Chang *et al.*, 2021] Minghui Chang, Xiangchao Meng, Weiwei Sun, Gang Yang, and Jiangtao Peng. Collaborative coupled hyperspectral unmixing based subpixel change detection for analyzing coastal wetlands. *IEEE Journal of Selected Topics in Applied Earth Observations and Remote Sensing*, 14:8208–8224, 2021.

[Chen and Shi, 2020] Hao Chen and Zhenwei Shi. A spatial-temporal attention-based method and a new dataset for remote sensing image change detection. *Remote Sensing*, 12(10):1662, 2020.

[Chen *et al.*, 2018] Zhao Chen, Vijay Badrinarayanan, Chen-Yu Lee, and Andrew Rabinovich. GradNorm: Gradient normalization for adaptive loss balancing in deep multitask networks. In *Proceedings of the 35th International Conference on Machine Learning, ICML 2018, Stockholmsmässan, Stockholm, Sweden, July 10-15, 2018*, volume 80, pages 793–802, 2018.

[Chen *et al.*, 2022] Hao Chen, Zipeng Qi, and Zhenwei Shi. Remote sensing image change detection with transformers. *IEEE Transactions on Geoscience and Remote Sensing*, 60:1–14, 2022.

[Chen *et al.*, 2023] Tianlong Chen, Xuxi Chen, Xianzhi Du, Abdullah Rashwan, Fan Yang, Huizhong Chen, Zhenyang Wang, and Yeqing Li. AdaMV-MoE: Adaptive multi-task vision mixture-of-experts. In *2023 IEEE/CVF International Conference on Computer Vision (ICCV)*, pages 17300–17311, 2023.

[Chen *et al.*, 2024] Hongruixuan Chen, Jian Song, Chengxi Han, Junshi Xia, and Naoto Yokoya. ChangeMamba: Remote sensing change detection with spatiotemporal state space model. *IEEE Transactions on Geoscience and Remote Sensing*, 62:1–20, 2024.

[Dong *et al.*, 2024] Sijun Dong, Libo Wang, Bo Du, and Xiaoliang Meng. ChangeCLIP: Remote sensing change detection with multimodal vision-language representation learning. *ISPRS Journal of Photogrammetry and Remote Sensing*, 208:53–69, 2024.

[Fang *et al.*, 2022] Sheng Fang, Kaiyu Li, Jinyuan Shao, and Zhe Li. SNUNet-CD: A densely connected siamese network for change detection of vhr images. *IEEE Geoscience and Remote Sensing Letters*, 19:1–5, 2022.

[Feng *et al.*, 2023] Yuchao Feng, Jiawei Jiang, Honghui Xu, and Jianwei Zheng. Change detection on remote sensing images using dual-branch multilevel intertemporal network. *IEEE Transactions on Geoscience and Remote Sensing*, 61:1–15, 2023.

[He *et al.*, 2016] Kaiming He, Xiangyu Zhang, Shaoqing Ren, and Jian Sun. Deep residual learning for image recognition. In *2016 IEEE Conference on Computer Vision and Pattern Recognition (CVPR)*, pages 770–778, 2016.

[Jaegle *et al.*, 2022] Andrew Jaegle, Sebastian Borgeaud, Jean-Baptiste Alayrac, Carl Doersch, Catalin Ionescu, David Ding, Skanda Koppula, Daniel Zoran, Andrew Brock, Evan Shelhamer, Olivier J. Hénaff, Matthew M. Botvinick, Andrew Zisserman, Oriol Vinyals, and João Carreira. Perceiver IO: A general architecture for structured inputs & outputs. In *The Tenth International Conference on Learning Representations, ICLR 2022, Virtual Event, April 25-29, 2022*. OpenReview.net, 2022.

[Jain *et al.*, 2024] Yash Jain, Harkirat Behl, Zsolt Kira, and Vibhav Vineet. DAMEX: Dataset-aware mixture-of-experts for visual understanding of mixture-of-datasets. *Advances in Neural Information Processing Systems*, 36, 2024.

[Jang *et al.*, 2017] Eric Jang, Shixiang Gu, and Ben Poole. Categorical reparameterization with gumbel-softmax. In *5th International Conference on Learning Representations, ICLR 2017, Toulon, France, April 24-26, 2017, Conference Track Proceedings*, 2017.

[Ji *et al.*, 2018] Shunping Ji, Shiqing Wei, and Meng Lu. Fully convolutional networks for multisource building extraction from an open aerial and satellite imagery data set. *IEEE Transactions on geoscience and remote sensing*, 57(1):574–586, 2018.

[Jiang and Wu, 2025] Kaixuan Jiang and Chen Wu. LGCANet: Local-global and change-aware network via segment anything model for remote sensing images change detection. *IEEE Transactions on Geoscience and Remote Sensing*, 63:1–13, 2025.

[Jing *et al.*, 2024] Wei Jing, Kaichen Chi, Qiang Li, and Qi Wang. 3-D Neighborhood Cross-Differencing: A new paradigm serves remote sensing change detection. *IEEE Transactions on Geoscience and Remote Sensing*, 62:1–11, 2024.

[Jing *et al.*, 2025] Wei Jing, Haichen Bai, Binbin Song, Weiping Ni, Junzheng Wu, and Qi Wang. Hetecd: Feature consistency alignment and difference mining for heterogeneous remote sensing image change detection. *ISPRS Journal of Photogrammetry and Remote Sensing*, 223:317–327, 2025.

[Li *et al.*, 2022] Zhenglai Li, Chang Tang, Lizhe Wang, and Albert Y. Zomaya. Remote sensing change detection via temporal feature interaction and guided refinement. *IEEE Transactions on Geoscience and Remote Sensing*, 60:1–11, 2022.

[Li *et al.*, 2023] Zhenglai Li, Chang Tang, Xinwang Liu, Wei Zhang, Jie Dou, Lizhe Wang, and Albert Y. Zomaya. Lightweight remote sensing change detection with progressive feature aggregation and supervised attention. *IEEE Transactions on Geoscience and Remote Sensing*, 61:1–12, 2023.

[Li *et al.*, 2024] Kaiyu Li, Xiangyong Cao, and Deyu Meng. A new learning paradigm for foundation model-based remote-sensing change detection. *IEEE Transactions on Geoscience and Remote Sensing*, 62:1–12, 2024.

[Li *et al.*, 2025a] Miao Li, Dongping Ming, Lu Xu, Dehui Dong, and Yu Zhang. SFEARNet: A network combining semantic flow and edge-aware refinement for highly efficient remote sensing image change detection. *IEEE Transactions on Geoscience and Remote Sensing*, 63:1–18, 2025.

[Li *et al.*, 2025b] Yuxuan Li, Xiang Li, Yunheng Li, Yicheng Zhang, Yimian Dai, Qibin Hou, Ming-Ming Cheng, and Jian Yang. SM3Det: A unified model for multi-modal remote sensing object detection, 2025.

[Liu *et al.*, 2020] Jiang-Jiang Liu, Qibin Hou, Ming-Ming Cheng, Changhu Wang, and Jiashi Feng. Improving convolutional networks with self-calibrated convolutions. In *2020 IEEE/CVF Conference on Computer Vision and Pattern Recognition (CVPR)*, pages 10093–10102, 2020.

[Lu *et al.*, 2025] Wei Lu, Si-Bao Chen, Chris H. Q. Ding, Jin Tang, and Bin Luo. LWGANet: A lightweight group attention backbone for remote sensing visual tasks, 2025.

[Mei *et al.*, 2024] Liye Mei, Zhaoyi Ye, Chuan Xu, Hongzhu Wang, Ying Wang, Cheng Lei, Wei Yang, and Yansheng Li. SCD-SAM: Adapting segment anything model for semantic change detection in remote sensing imagery. *IEEE Trans. Geosci. Remote. Sens.*, 62:1–13, 2024.

[Noman *et al.*, 2024] Mubashir Noman, Mustansar Fiaz, Hisham Cholakkal, Salman H. Khan, and Fahad Shahbaz Khan. ELGC-Net: Efficient local-global context aggregation for remote sensing change detection. *IEEE Transactions on Geoscience and Remote Sensing*, 62:1–11, 2024.

[Pu *et al.*, 2024] Yan Pu, Maoguo Gong, Tongfei Liu, Mingyang Zhang, Tianqi Gao, Fenlong Jiang, and Xiaobo Hu. Adversarial feature equilibrium network for multi-modal change detection in heterogeneous remote sensing images. *IEEE Transactions on Geoscience and Remote Sensing*, 62:1–17, 2024.

[Shao *et al.*, 2021] Ruizhe Shao, Chun Du, Hao Chen, and Jun Li. SUNet: Change detection for heterogeneous remote sensing images from satellite and uav using a dual-channel fully convolution network. *Remote Sensing*, 13(18), 2021.

[Shazeer *et al.*, 2017] Noam Shazeer, Azalia Mirhoseini, Krzysztof Maziarz, Andy Davis, Quoc V. Le, Geoffrey E. Hinton, and Jeff Dean. Outrageously large neural networks: The sparsely-gated mixture-of-experts layer. In *5th International Conference on Learning Representations, ICLR 2017, Toulon, France, April 24-26, 2017, Conference Track Proceedings*, 2017.

[Shu *et al.*, 2024] Qing-Ling Shu, Si-Bao Chen, Zhi-Hui You, Jin Tang, and Bin Luo. Prior guidance and principal attention network for remote sensing image change detection. *IEEE Transactions on Geoscience and Remote Sensing*, 62:1–13, 2024.

[Wang *et al.*, 2021] Dequan Wang, Evan Shelhamer, Shaoteng Liu, Bruno A. Olshausen, and Trevor Darrell. Tent: Fully test-time adaptation by entropy minimization. In *9th International Conference on Learning Representations, ICLR 2021, Virtual Event, Austria, May 3-7, 2021*. OpenReview.net, 2021.

[Wang *et al.*, 2025a] Di Wang, Guorui Ma, Haiming Zhang, Xiao Wang, and Yongxian Zhang. Refined change detection in heterogeneous low-resolution remote sensing images for disaster emergency response. *ISPRS Journal of Photogrammetry and Remote Sensing*, 220:139–155, 2025.

[Wang *et al.*, 2025b] Guangxing Wang, Gong Cheng, and Junwei Han. Change detection mamba with boundary-specific supervision. *IEEE Transactions on Circuits and Systems for Video Technology*, pages 1–1, 2025.

[Yang *et al.*, 2024] Yuqi Yang, Peng-Tao Jiang, Qibin Hou, Hao Zhang, Jinwei Chen, and Bo Li. Multi-task dense prediction via mixture of low-rank experts. In *2024 IEEE/CVF Conference on Computer Vision and Pattern Recognition (CVPR)*, pages 27927–27937, 2024.

[You *et al.*, 2023] Zhi-Hui You, Jia-Xin Wang, Si-Bao Chen, Chris H. Q. Ding, Gui-Zhou Wang, Jin Tang, and Bin Luo. Crossed siamese vision graph neural network for remote-sensing image change detection. *IEEE Transactions on Geoscience and Remote Sensing*, 61:1–16, 2023.

[Zhang *et al.*, 2022] Chenxiao Zhang, Yukang Feng, Lei Hu, Deodato Tapete, Li Pan, Zheheng Liang, Francesca Cigna, and Peng Yue. A domain adaptation neural network for change detection with heterogeneous optical and sar remote sensing images. *International Journal of Applied Earth Observation and Geoinformation*, 109:102769, 2022.

[Zhang *et al.*, 2025] Haotian Zhang, Keyan Chen, Chenyang Liu, Hao Chen, Zhengxia Zou, and Zhenwei Shi. CD-Mamba: Incorporating local clues into mamba for remote sensing image binary change detection, 2025.

[Zhao *et al.*, 2025] Jingyu Zhao, Jiahui Qu, and Wenqian Dong. Bi-DiffCD: Bidirectional diffusion guided collaborative change detection for arbitrary-modal remote sensing images. In *Proceedings of the Thirty-Fourth International Joint Conference on Artificial Intelligence, IJCAI-25*, pages 2449–2457, 8 2025.

[Zheng *et al.*, 2025] Zhuo Zheng, Stefano Ermon, Dongjun Kim, Liangpei Zhang, and Yanfei Zhong. Changen2: Multi-temporal remote sensing generative change foundation model. *IEEE Transactions on Pattern Analysis and Machine Intelligence*, 47(2):725–741, 2025.